

**The following resources related to this article are available online at [www.sciencemag.org](http://www.sciencemag.org) (this information is current as of September 21, 2009 ):**

**Updated information and services**, including high-resolution figures, can be found in the online version of this article at:

<http://www.sciencemag.org/cgi/content/full/325/5946/1371>

**Supporting Online Material** can be found at:

<http://www.sciencemag.org/cgi/content/full/325/5946/1371/DC1>

This article **cites 27 articles**, 3 of which can be accessed for free:

<http://www.sciencemag.org/cgi/content/full/325/5946/1371#otherarticles>

This article appears in the following **subject collections**:

Geochemistry, Geophysics

[http://www.sciencemag.org/cgi/collection/geochem\\_phys](http://www.sciencemag.org/cgi/collection/geochem_phys)

Information about obtaining **reprints** of this article or about obtaining **permission to reproduce this article** in whole or in part can be found at:

<http://www.sciencemag.org/about/permissions.dtl>

the radial breathing mode (RBM) energy  $E_{\text{RBM}} \sim 7meV/d$  nm ( $I$ , 2) and other low-energy radial phonons. Indeed, recent optical measurements of the relaxation process  $E_{22} \rightarrow E_{11}$  have suggested strong exciton-phonon coupling to the SWNT radial breathing mode at room temperature (22). Although the low temperature onset of impact excitation is comparable to the freeze-out of RBM phonons ( $T < E_{\text{RBM}}/k_B \sim 80$  K), other processes may be responsible.

The impact excitation process  $e_2 + K_e \rightarrow e_1 + n(e_1 + h_1)$  differs strongly from impact ionization observed in traditional semiconductors in two important ways. First, no avalanche breakdown behavior is observed here because hot  $\varepsilon_2$  carriers create  $\varepsilon_1$  carriers, which do not undergo additional multiplication at low reverse bias (see SOM text). Second, the process observed here is extremely efficient, occurring as soon as it is energetically allowed. In standard semiconductors, competing loss mechanisms restrict impact excitation to extremely large biases (18).

These results also differ strongly from previous theory and experiments on SWNTs. Perebeinos *et al.* (23) calculated that single-particle impact excitation in SWNTs should be highly efficient, but only in the third subband and higher because of momentum conservation transverse to the tube axis. We observed a highly efficient process in the second subband, suggesting that either other carriers or phonons are involved to conserve momentum. Earlier experiments on SWNT transistors attributed bright electroluminescence (5–7) and avalanche breakdown (24) (see SOM text) to electron-hole generation by impact excitation, but as with traditional semiconductors, these processes were only observed

at large biases, and the importance of the subband index was not discussed.

The e-h pair creation process observed here may make possible increased power conversion efficiency in future photovoltaic devices. The standard limit of photovoltaic efficiency, first established by Shockley and Queisser (11), is set by the conversion of a single photon into a single e-h pair. In the SWNT p-n junction, a single photon with energy  $E_{\text{PHOTON}} > E_{22}$  is converted into multiple e-h pairs, leading to enhanced photocurrent and increased efficiency. Evidence for a related process, known as multiple exciton generation (MEG) (10, 12–14), has been observed in various semiconductor nanocrystals, but these observations remain controversial, and improved photovoltaic device behavior has not been demonstrated. The results presented here clearly show that multiple e-h pairs can be generated and collected in a nanotube p-n junction. Although implementation of devices exploiting e-h pair generation into photovoltaic cells will require substantial future effort, the process observed here has substantial implications for such technology and represents a very important step toward ultra-efficient photovoltaic devices with power conversion efficiency exceeding the Shockley-Queisser limit.

#### References and Notes

1. R. Saito, G. Dresselhaus, M. S. Dresselhaus, *Physical Properties of Carbon Nanotubes* (Imperial College, London, 1998).
2. P. Avouris, Z. Chen, V. Perebeinos, *Nat. Nanotechnol.* **2**, 605 (2007).
3. O. Hayden, R. Agarwal, C. M. Lieber, *Nat. Mater.* **5**, 352 (2006).
4. C. Yang, C. J. Barrelet, F. Capasso, C. M. Lieber, *Nano Lett.* **6**, 2929 (2006).

5. J. A. Misewich *et al.*, *Science* **300**, 783 (2003).
6. J. Chen *et al.*, *Science* **310**, 1171 (2005).
7. L. Marty *et al.*, *Phys. Rev. Lett.* **96**, 136803 (2006).
8. B. Tian *et al.*, *Nature* **449**, 885 (2007).
9. J. U. Lee, *Appl. Phys. Lett.* **87**, 073101 (2005).
10. R. D. Schaller, V. I. Klimov, *Phys. Rev. Lett.* **92**, 186601 (2004).
11. W. Shockley, H. J. Queisser, *J. Appl. Phys.* **32**, 510 (1961).
12. R. J. Ellington *et al.*, *Nano Lett.* **5**, 865 (2005).
13. J. Kim *et al.*, *Appl. Phys. Lett.* **92**, 031107 (2008).
14. R. D. Schaller, V. M. Agranovich, V. I. Klimov, *Nat. Phys.* **1**, 189 (2005).
15. J. U. Lee, P. Gipp, C. M. Heller, *Appl. Phys. Lett.* **85**, 145 (2004).
16. K. Bosnick, N. M. Gabor, P. L. McEuen, *Appl. Phys. Lett.* **89**, 163121 (2006).
17. Materials and methods are available as supporting material on Science Online.
18. S. M. Sze, *Physics of Semiconductor Devices* (Wiley, London, ed. 2, 1981).
19. E. Pop *et al.*, *Phys. Rev. Lett.* **95**, 155505 (2005).
20. J. Y. Park *et al.*, *Nano Lett.* **4**, 517 (2004).
21. Z. Yao, C. L. Kane, C. Dekker, *Phys. Rev. Lett.* **84**, 2941 (2000).
22. C. Manzoni *et al.*, *Phys. Rev. Lett.* **94**, 207401 (2005).
23. V. Perebeinos, P. Avouris, *Phys. Rev. B* **74**, 121410 (2006).
24. A. Liao, Y. Zhao, E. Pop, *Phys. Rev. Lett.* **101**, 256804 (2008).
25. We thank R. Ilic and J. Kinder for useful discussions. This work was supported by the NSF through the Center for Nanoscale Systems and by the Microelectronics Advanced Research Corporation Focused Research Center on Materials, Structures, and Devices. Sample fabrication was performed at the Cornell Nanoscale Science and Technology Facility, a National Nanotechnology Infrastructure Network node, funded by NSF.

#### Supporting Online Material

www.sciencemag.org/cgi/content/full/325/5946/1367/DC1  
Materials and Methods  
SOM Text  
Figs. S1 to S3  
References

11 May 2009; accepted 13 July 2009  
10.1126/science.1176112

## Underplating in the Himalaya-Tibet Collision Zone Revealed by the Hi-CLIMB Experiment

John Nábělek,<sup>1\*</sup> György Hetényi,<sup>2†</sup> Jérôme Vergne,<sup>2‡</sup> Soma Sapkota,<sup>3</sup> Basant Kafle,<sup>3§</sup> Mei Jiang,<sup>4</sup> Heping Su,<sup>4</sup> John Chen,<sup>5</sup> Bor-Shouh Huang,<sup>6</sup> the Hi-CLIMB Team||

We studied the formation of the Himalayan mountain range and the Tibetan Plateau by investigating their lithospheric structure. Using an 800-kilometer-long, densely spaced seismic array, we have constructed an image of the crust and upper mantle beneath the Himalayas and the southern Tibetan Plateau. The image reveals in a continuous fashion the Main Himalayan thrust fault as it extends from a shallow depth under Nepal to the mid-crust under southern Tibet. Indian crust can be traced to 31°N. The crust/mantle interface beneath Tibet is anisotropic, indicating shearing during its formation. The dipping mantle fabric suggests that the Indian mantle is subducting in a diffuse fashion along several evolving subparallel structures.

The collision of the Indian tectonic plate with Eurasia is the primary force behind the rise of the Himalayan mountain range and the uplift of the Tibetan Plateau. The Indian lithosphere has been underthrusting beneath Tibet since the closing of the Tethys Sea in the early

Tertiary, and the mountain-building deformation front has moved southward from the initial collision contact at the Yarlung Tsangpo Suture by processes that transfer Indian crust to the overriding plate. Seismological studies [such as (1–4)] have shown that the Indian plate continues to underthrust southern

Tibet at least up to the south Lhasa Block, but its northern limit and geometry are still uncertain (5).

Here we present a high-resolution continuous cross section of lithospheric interfaces through the Himalayas and the southern half of the Tibetan Plateau constructed from seismological data acquired in 2002–2005 by the project Hi-CLIMB

<sup>1</sup>College of Oceanic and Atmospheric Sciences, Oregon State University, Corvallis, OR 97331, USA. <sup>2</sup>Laboratoire de Géologie, École Normale Supérieure, CNRS-UMR 8538, 24 Rue Lhomond, 75005 Paris, France. <sup>3</sup>National Seismological Center, Department of Mines and Geology, Kathmandu, Nepal. <sup>4</sup>Institute of Geology, Chinese Academy of Geological Sciences, Beijing, People's Republic of China (PRC). <sup>5</sup>Institute of Theoretical and Applied Geophysics, Peking University, Beijing, PRC. <sup>6</sup>Institute of Earth Sciences, Academia Sinica, Taipei, Taiwan.

\*To whom correspondence should be addressed. E-mail: nabelek@coas.oregonstate.edu

†Present address: Earth Sciences Department, ETH Zurich, 8092 Zurich, Switzerland.

‡Present address: Ecole et Observatoire des Sciences de la Terre, CNRS-UMR 7516, 5 rue René Descartes, 67084 Strasbourg, France.

§Present address: Alberta Geological Survey, 4999-98 Avenue, Edmonton, Alberta T6B 2X3, Canada.

||All additional authors with their affiliations appear at the end of this paper.

(Himalayan-Tibetan Continental Lithosphere During Mountain Building) (6). The centerpiece of the project was a closely spaced, 800-km-long linear array of broadband seismometers extending northward from the Ganges Basin, across the Himalayas, the Yarlung Tsangpo Suture (YTS), and the Banggong-Nuijiang Suture (BNS) to central Tibet (Fig. 1). A sparser network of stations in Nepal and southern Tibet flanked the main linear array.

We focus on the images of the crust and upper mantle obtained along the main profile using the receiver function method (7). The receiver functions enhance converted *S* waves from *P* waves of distant earthquakes impinging on interfaces beneath the recording stations. A converted *PS* wave follows the direct *P* wave with a delay proportional to the depth of the converting interface and the average velocity structure above it (fig. S1). To produce a depth section, the wave conversions are “migrated” to their locations under the array using a two-dimensional (2D) velocity model (8). In order to minimize the influence of interference from shallow layers, we combine the image of migrated *PS* conversions with the images of migrated *PpS* and *PsS* (*p*, *P*-wave reflection from the free surface; *s*, *S*-wave reflection from the free surface; fig. S1) multiples to produce the final image, which enhances the wavefield to be coherent in all three images (8).

Several resolvable features in this image help construct the geometry of the Indian crust beneath Tibet. The crust/mantle boundary, or Moho, is a prominent positive conversion seen along the entire profile (Fig. 2A). In the south, it dips gently from a depth of 40 km beneath the Ganges Basin on the Indian Plate to 50 km beneath the Himalayas. North of the Great Himalaya, from about 150 km north of the Main Frontal thrust (MFT), the Moho deepens more rapidly, reaching a depth of 70 km north of the YTS (250 km north from the MFT). From this point, in the Lhasa Block, the Moho signal is at a constant depth over the next 200 km. Here, another prominent interface lies 15 km above the Moho. Farther north, this interface merges with the Moho, and the Moho becomes less clearly defined. The Moho reappears as a strong interface north of the BNS, under the Qiangtang Block, but at a shallower depth of about 65 km.

These changes in crustal thickness do not correlate with the topography in the region between the Greater Himalaya and the YTS (Fig. 2A). This lack of relation indicates that the area is in regional isostatic compensation involving high-density (high-velocity) lower crust and mantle (9, 10) and support from the flexural strength of the Indian plate (11). The thinner crust of the Qiangtang Block (12) appears to be compensated for by a lower-density and lower-velocity mantle (9, 10) and thus is distinctly different from the southern Lhasa Block.

We interpret the 15-km-thick layer above the Moho in the southern Lhasa Block [also observed by (9)] as the underplated lower crust of India. The layer is characterized by a strong velocity-depth gradient (Fig. 2D) and can be traced, albeit much less clearly, to shallower depths under

Nepal. On the basis of gravity anomalies, this lower-crustal layer, probably of amphibolitic composition beneath Nepal, has been at least partially transformed into eclogite because of high-grade metamorphic reactions [for details, see (13)].

The Main Himalayan thrust (MHT) fault, the detachment along which the Indian plate descends beneath the Himalayas and southern Tibet, follows the continuous blue feature in Fig. 2 (corresponding to a velocity decrease with depth), extending from shallow depths under Nepal to mid-crustal depths in the Lhasa Block. Beneath Nepal, the MHT partially underthrusts low-velocity sediments from the Ganges Basin under the Lesser Himalaya formations (14). The sharp velocity decrease associated with this part of the MHT possibly reflects the presence of water released from the underthrust sediments and trapped beneath by clay-bearing fault gouge. The induced overpressure of the trapped fluid decreases the fault strength and enables low-angle thrusting in this zone characterized by large earthquakes. In contrast, the velocity decrease associated with the deeper, creeping section of the MHT is probably caused by increased ductility and local partial melting (15). The presence of fluids or partial melt in both low-velocity zone (LVZ) segments is supported by low electrical resistivity measurements (16–18). North of the YTS, in the Lhasa Block, the MHT becomes horizontal (Fig. 2, A and D). As it is along its dipping portion, it is presumably ductile here.

Some features are more difficult to interpret from Fig. 2. For example, the uppermost 10 km of the crust is partly contaminated by mismigrated *PS* conversions introduced during data processing (8). The *PS* image alone (fig. S2) shows the presence of shallow features of limited horizontal extent (<50 km). These features share similarities in terms of depth, extent, and polarity with the “bright spots” observed by reflection seismology in southern Tibet (19) and interpreted as lenses of fluid. However, they clearly do not form the top of a partially molten middle and lower crust as has been suggested (2). The average crustal  $V_P/V_S$  ratio ( $V$ , wave speed) beneath both southern and central Tibet exhibits low to regular values (fig. S2), indicating that the crust does not contain widespread partial melt (9).

The *PS* conversion at the Moho for the *P* waves arriving from the north and south is distinctly different. The Moho is sharp beneath the Lhasa Block south of 31°N when illuminated from the north (Fig. 2B) but shows a weak incoherent image when illuminated from the south (Fig. 2C). On the other hand, the Moho north of 31°N is almost invisible from the north, whereas it is clearly visible from the south. *P* waves are converted to *S* waves when the *P* waves approach an interface obliquely but not when they arrive perpendicularly. The nearly invisible Moho signatures imply that lower-crustal interfaces are perpendicular to the corresponding arriving waves. Therefore, the lower crustal structure of the Lhasa Block is

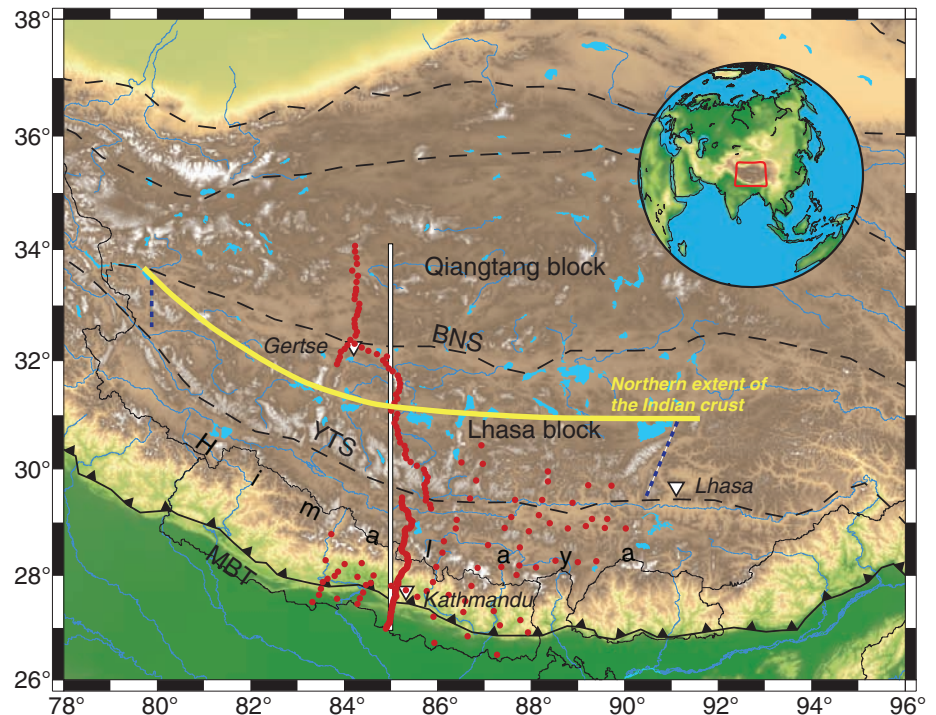


**Fig. 1.** The layout of the Hi-CLIMB experiment in Nepal and on the Tibetan Plateau. Red circles indicate the positions of broadband seismological stations. The white vertical line is the location of the projected cross section shown in Fig. 2. Barbed and dashed black lines mark major fault zones and sutures separating main tectonic blocks: the Main Boundary thrust (MBT), YTS, and BNS. The yellow line shows the inferred northern limit of the underplated lower crust of the Indian plate. Blue dashed lines show locations of lower crust duplexes observed in other receiver function studies (9, 26).

dipping to the north [see also (20)], whereas that of the region north of 31°N is dipping to the south.

The arrival times of the converted phases at the Moho north of the YTS indicate nearly horizontal geometry, hence the apparent dip implied by the *PS* amplitudes probably results from a strong velocity anisotropy in the lowermost crust. An alignment of crystals or mylonites induced by a ductile flow, commonly assumed to be responsible for seismic velocity anisotropy, is probably not the cause here because the measured anisotropy in eclogites is less than 4% (21). A more likely alternative is a macroscale fabric developed by imbrication and rotation of initially vertically stratified lower crust. This imbrication fabric may have formed as the lower crust negotiated the sharp bend at the YTS. Decoupling and shearing between the lower crust and the mantle while the Indian plate bends have been also suggested by numerical modeling (11). Furthermore, the 10% volume decrease associated with conversion to eclogite (13) may aid the imbrication.

The receiver function image also indicates the northward limit of the Indian plate. The MHT extends uninterrupted from Nepal into a mid-crustal LVZ observed across the southern Lhasa Block. The Indian lower crust exhibits high velocities beneath the Himalayas (2, 22); these extend horizontally beneath the Tibetan Plateau up to about 31°N. The 31°N boundary appears also to extend deeper into the uppermost mantle. In the mantle, the migrated images (Fig. 2D and fig. S4) reveal several faint lineations, which suggest that it has been deforming in a distributed fashion. The most prominent lineations have similar vergence as that we have inferred for the lower crust, dipping primarily northward south of 31°N (at about a 20° angle) and southward (at a somewhat steeper angle) north of this region. A north-dipping reflectivity fabric down to a depth of 150 km in the mantle has also been observed in high-frequency seismic reflection data near here (23).

These sharp differences in the seismic characteristics of the lower crust and uppermost mantle

suggest that the zone located north of 31°N and south of the BNS is a boundary between two lithospheric-scale blocks: To the south beneath the Tibetan upper crust is the Indian plate, and to the north is the Eurasian plate. As suggested by the convergence of the mantle lineations, a mantle downwelling could have occurred along this boundary. Seismic travel-time tomography east of our profile (24) shows a vertical high-velocity body between depths of 200 and 400 km, roughly equivalent to the region of converging lineations we imaged. S-SE dipping features beneath the Qiangtang Block also have been observed to the east of our profile, where they have been interpreted to represent the ongoing descent of the Eurasian lithosphere (25).

The characteristic duplex of strong conversions at the top and bottom of the lower crustal layer beneath the Lhasa Block, interpreted to belong to the Indian plate, can also be observed in eastern and western Tibet (9, 26) and provide lateral constraints on the position of the plate

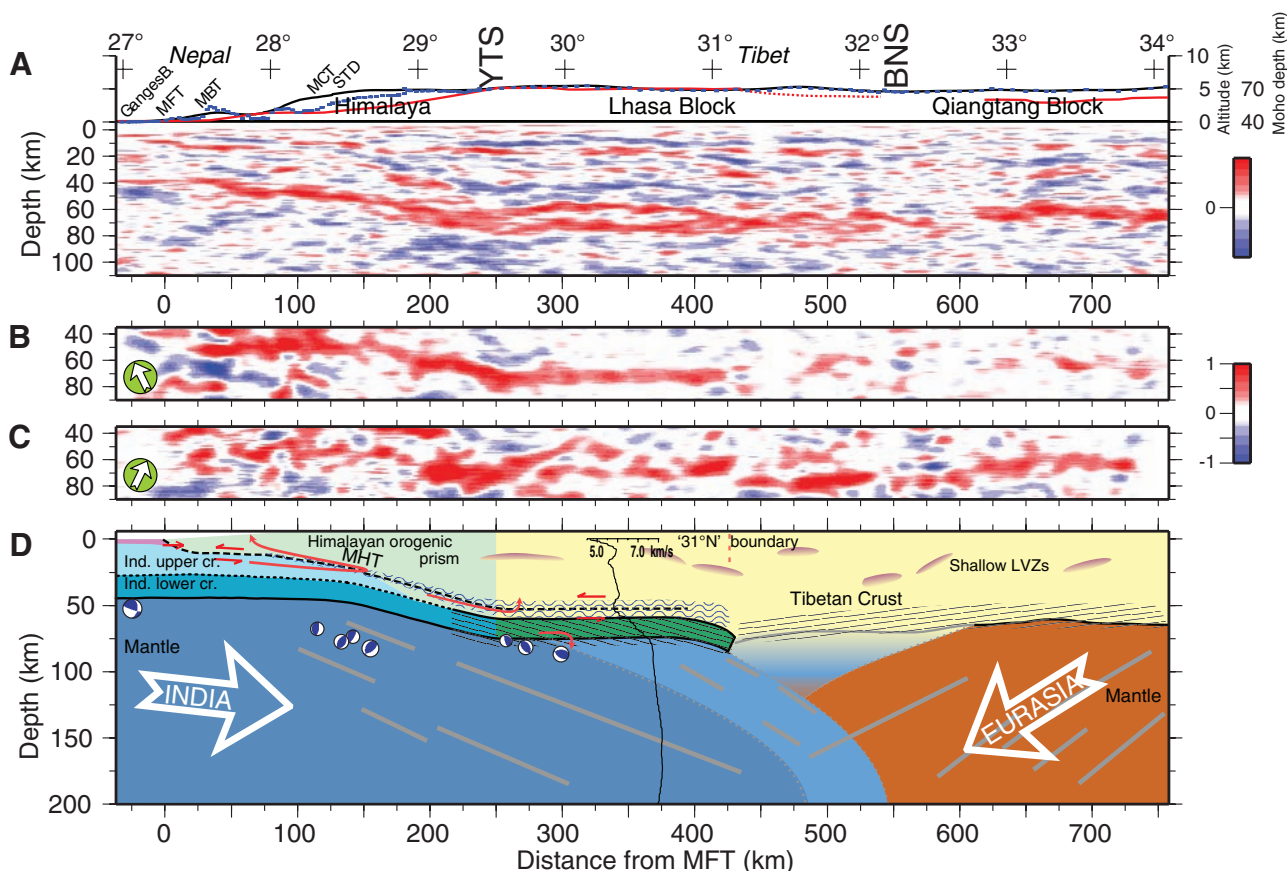


**Fig. 2.** (A) Receiver function image along the main profile showing the principal contrasts within the lithosphere (red and blue colors represent interfaces with increasing and decreasing impedance with depth, respectively). The horizontal distances are referenced to the MFT. All depths are relative to sea level. The top of the figure shows the station altitude (blue dashes), average topography (black line), and Moho depth (red line). To determine the crustal thickness, one must add topography to the observed Moho depth. (B) Image of the Moho using northward illumination by the *PS* phases. (C) Same as in (B) but illuminated from the south. (D) Interpretative cross section of the India-Eurasia collision zone. The lower part of the Indian lithosphere underplates the Himalayas and Tibet up to 31°N.

The eclogitized lower crust is shown in green. Moho conversion is shown by a black line when it is strong and a gray line when it is weak. The approximate dip of the inferred opposing lower crustal fabric is indicated by thin lines. Focal mechanisms mark mantle earthquakes (32). The MHT, which becomes a broader mid-crustal LVZ (blue wavy pattern) in the southern Lhasa Block, accommodates the simple shear of the plate motions and acts as a conduit for the transfer of the Indian upper crust into the Himalayan orogenic prism (red arrows). The prominent lineations of the upper mantle fabric are shown in gray. The average *P*-wave velocity depth profile for the southern Lhasa Block determined by receiver function waveform inversion is also shown (black line).

(Fig. 1). The northern limit of the observed duplexes runs approximately parallel to the Himalayan arc. This limit also corresponds to a sharp change in the velocity and attenuation of  $P_n$  and  $S_n$  (refracted  $P$  and  $S$  along Moho) waves (9, 27) and is observed in tomographic images (4) where it marks the northern extent of higher-than-average mantle velocities. Along the Lhasa-Golmud road, the presumed northern limit of the Indian lower crust marks an increase in the amount of shear-wave splitting (28). Although the structures we have imaged are largely consistent with collisional tectonics, the sharp change in the directionality of the Moho conversions north and south of 31°N, as well as the sharp onset of these other geophysical observables, suggests that some strike-slip motion has also occurred along the boundary.

Our data do not provide unequivocal evidence for active channel flow (29) because the zones we interpret as ductile are too thin to allow vigorous flow. Examining the thickness of the Indian crustal layers provides constraints on the processes involving mass transfer from the Indian crust into the Himalayan orogenic prism and the Tibetan crust. The Indian uppermost crust is presumably transferred to the Himalayan orogenic prism by southward progression of the leading listric thrust faults (currently the MFT) extending to the surface from the detachment (the MHT). The Indian upper crust does not appear to be underplated under the Lhasa Block, which indicates that the ductile part of the MHT not only takes up the simple shear of the plate motions but also acts as a conduit for crustal transfer. The likely places for mass transfer processes [partly from (30)] are shown in Fig. 2D by red arrows. The ductile (upward) mass transfer processes, depending on the details, may result in a crustal extrusion along the STD and/or out-of-sequence thrusting at the Main Central Thrust or other thrust sheets (Fig. 2A). In addition to the upward mass transfer, there is a possibility that eclogitized Indian lower crust is being absorbed into the mantle.

The signatures of the MHT and the Indian lower crust extend about 450 km northward from the MFT. Recent global positioning system measurements indicate that India now underthrusts the Himalayas at the rate of 1.7 to 2 cm/year (30). This suggests that the observed underplating has developed in less than 20 to 25 million years, which is about half of the age of collision. A plausible explanation could be that the missing (older) lower crust was subducted together with the Indian lithospheric mantle at the earlier stage of the collision (9). The opposing upper-mantle fabrics (Fig. 2D) indicate that the Indian mantle lithosphere has not extended significantly beyond 31°N and that, at least in the past, the Indian plate subduction was substantially steeper (31). The mantle fabric also suggests that in the past 20 to 25 million years, the mantle has not been subducting along a single well-established interface but rather along distributed evolving subparallel structures.

This distributed mantle deformation implies a degree of decoupling between the crust and the

mantle. The presence of mantle earthquakes indicates that the mantle is actively deforming (Fig. 2D). The polarized  $PS$  conversions over the entire profile north of the YTS suggest that mantle-crust decoupling (shear) may be ubiquitous under Tibet and may be an integral part of the process of building the doubly thickened Tibetan crust.

#### References and Notes

1. A. Hirn *et al.*, *Nature* **307**, 25 (1984).
2. K. D. Nelson *et al.*, *Science* **274**, 1684 (1996).
3. V. Schulte-Pelkum *et al.*, *Nature* **435**, 1222 (2005).
4. C. Li *et al.*, *Earth Planet. Sci. Lett.* **274**, 157 (2008).
5. S. Klemperer, [www.gsjournals.org](http://www.gsjournals.org), 10.1130/G25097C.1 (2008).
6. The Hi-CLIMB network included 75 broadband seismic stations from the U.S. Program for Array Seismic Studies of the Continental Lithosphere (PASSCAL), supplemented in southern Tibet by 32 stations from Peking University and the Chinese Academy of Geological Sciences, PRC; and from the Academia Sinica, Taiwan. Throughout the experiment, the stations occupied 233 locations.
7. C. Langston, *J. Geophys. Res.* **84**, 4749 (1979).
8. Methods are discussed in the supporting material on Science Online.
9. R. Kind *et al.*, *Science* **298**, 1219 (2002).
10. A. J. Rodgers, S. Y. Schwartz, *Geophys. Res. Lett.* **24**, 9 (1997).
11. G. Hetényi, R. Cattin, J. Vergne, J. L. Nábělek, *Geophys. J. Int.* **167**, 1106 (2006).
12. X. Kong, Q. Wang, S. Xiong, *Chin. Sci. Bull.* **44**, 2022 (1999).
13. G. Hetényi *et al.*, *Earth Planet. Sci. Lett.* **264**, 226 (2007) and references therein.
14. P. G. DeCelles *et al.*, *Tectonics* **20**, 487 (2001).
15. J. Vergne, J. L. Nábělek, *Eos* **86** (Fall Meet. Suppl.), abstr. T52A-03 (2005).
16. C. Lemonnier *et al.*, *Geophys. Res. Lett.* **26**, 3261 (1999).
17. M. J. Unsworth *et al.*, *Nature* **438**, 78 (2005).
18. P. K. Patro, T. Harinarayana, *Phys. Earth Planet. Inter.* **173**, 171 (2009).
19. Y. Makovsky, S. L. Klemperer, *J. Geophys. Res.* **104**, 10795 (1999).
20.  $PS$  polarization at the Moho in the southern Lhasa Block has also been reported by INDEPTH II (5, 33).
21. V. Babuska, *Geophys. J. R. Astron. Soc.* **76**, 113 (1982).
22. G. Monsalve *et al.*, *J. Geophys. Res.* **111**, B10301 (2006).

23. D. Alsdorf, L. Brown, D. Nelson, *J. Geophys. Res.* **101**, 25305 (1996).
24. F. Tilmann, J. Ni, INDEPTH III Seismic Team, *Science* **300**, 1424 (2003).
25. D. Shi *et al.*, *Geology* **32**, 209 (2004).
26. G. Wittlinger *et al.*, *Earth Planet. Sci. Lett.* **221**, 117 (2004).
27. M. Barazangi, J. Ni, *Geology* **10**, 179 (1982).
28. W.-P. Chen, S. Ozalaybey, *Geophys. J. Int.* **135**, 93 (1998).
29. C. Beaumont *et al.*, *J. Geophys. Res.* **109**, B06406 (2004).
30. L. Bollinger, P. Henry, J.-P. Avouac, *Earth Planet. Sci. Lett.* **244**, 58 (2006).
31. S. Guillot *et al.*, *Geochem. Geophys. Geosyst.* **4**, 1064 (2003).
32. W.-P. Chen, Z. H. Yang, *Science* **304**, 1949 (2004).
33. J. Nabelek *et al.*, *Eos* **75** (Fall Meet. Suppl.), 628 (1994).
34. The Hi-CLIMB team was supported by the U.S. NSF, Continental Dynamics Program, grant EAR 9909609. The fieldwork was also supported in part by the Department of Mines and Geology, Nepal; the Chinese Academy of Geological Sciences and Peking University; and the Institute of Earth Sciences, Academia Sinica, Taiwan. G.H.'s thesis (<http://tel.archives-ouvertes.fr/tel-00194619/en/>) was supported by the French program DyETI. We acknowledge W.-P. Chen for the contribution to the planning of the experiment.

#### Project Hi-CLIMB Team

L. Mitchell,<sup>1</sup> D. Sherstad,<sup>1</sup> M. Arsenault,<sup>1</sup> J. Baur,<sup>1</sup> S. Carpenter,<sup>1</sup> M. Donahue,<sup>2</sup> D. Myers,<sup>1</sup> T.-L. Tseng,<sup>2</sup> T. Bardell,<sup>2</sup> N. VanHoudnos,<sup>2</sup> M. Pandey,<sup>3</sup> G. Chitrakar,<sup>3</sup> S. Rajauri,<sup>3</sup> G. Xue,<sup>4</sup> Y. Wang,<sup>4</sup> S. Zhou,<sup>5</sup> X. Liang,<sup>7</sup> G. Ye,<sup>3</sup> C.-C. Liu,<sup>6</sup> J. Lin,<sup>6</sup> C.-L. Wu,<sup>6</sup> N. Barstow<sup>7</sup>

<sup>1</sup>College of Oceanic and Atmospheric Sciences, Oregon State University, Corvallis, OR, USA. <sup>2</sup>Department of Geology, University of Illinois at Urbana-Champaign, Urbana, IL, USA. <sup>3</sup>Department of Mines and Geology, Kathmandu, Nepal. <sup>4</sup>Institute of Geology, Chinese Academy of Geological Sciences, Beijing, PRC. <sup>5</sup>Institute of Theoretical and Applied Geophysics, Peking University, Beijing, PRC. <sup>6</sup>Institute of Earth Sciences, Academia Sinica, Taipei, Taiwan. <sup>7</sup>PASSCAL, Socorro, NM, USA.

#### Supporting Online Material

[www.sciencemag.org/cgi/content/full/325/5946/1371/DC1](http://www.sciencemag.org/cgi/content/full/325/5946/1371/DC1)

Methods  
Figs. S1 to S4

References  
21 April 2009; accepted 27 July 2009  
10.1126/science.1167719

## Dynamic Processes Governing Low-Tropospheric HDO/H<sub>2</sub>O Ratios as Observed from Space and Ground

Christian Frankenberg,<sup>1\*</sup> Kei Yoshimura,<sup>2</sup> Thorsten Warneke,<sup>3</sup> Ilse Aben,<sup>1</sup> André Butz,<sup>1</sup> Nicholas Deutscher,<sup>4</sup> David Griffith,<sup>4</sup> Frank Hase,<sup>5</sup> Justus Notholt,<sup>3</sup> Matthias Schneider,<sup>5</sup> Hans Schrijver,<sup>1</sup> Thomas Röckmann<sup>6</sup>

The hydrological cycle and its response to environmental variability such as temperature changes is of prime importance for climate reconstruction and prediction. We retrieved deuterated water/water (HDO/H<sub>2</sub>O) abundances using spaceborne absorption spectroscopy, providing an almost global perspective on the near-surface distribution of water vapor isotopologs. We observed an unexpectedly high HDO/H<sub>2</sub>O seasonality in the inner Sahel region, pointing to a strong isotopic depletion in the subsiding branch of the Hadley circulation and its misrepresentation in general circulation models. An extension of the analysis at high latitudes using ground-based observations of  $\delta\bar{D}$  and a model study shows that dynamic processes can entirely compensate for temperature effects on the isotopic composition of precipitation.

Water vapor is the most important greenhouse gas in the atmosphere. As saturation vapor pressure increases exponentially with temperature, a positive feed-

back effect with respect to the current global warming trend is expected and confirmed by satellite measurements over the ocean (1–4). However, highly complex interactions via cloud



## Supporting Online Material for

### **Underplating in the Himalaya-Tibet Collision Zone Revealed by the Hi-CLIMB Experiment**

John Nábělek,\* György Hetényi, Jérôme Vergne, Soma Sapkota, Basant Kafle, Mei Jiang, Heping Su, John Chen, Bor-Shouh Huang, the Hi-CLIMB Team

\*To whom correspondence should be addressed. E-mail: nabelek@coas.oregonstate.edu

Published 11 September 2009, *Science* **325**, 1371 (2009)  
DOI: 10.1126/science.1167719

**This PDF file includes:**

Methods  
Figs. S1 to S4  
References

## Supporting Online Material

**Quality control and data selection.** As a result of the large number of deployed seismometers and the 3-year duration of the Hi-CLIMB project, the number of receiver functions computed exceeds 200,000. As it is impossible to visually analyze all of them, an automatic selection process was established and calibrated on a partial dataset to eliminate low quality events. The selection process included: 1) selection of  $M \geq 5.5$  events in the epicentral distance range of 30-95°; 2) exclusion of numerous small aftershocks closely following large magnitude events; 3) exclusion of traces based on signal-to-noise ratio of the original three-component data; 4) automatic examination of the receiver function shape based on the time of its peak amplitude; 5) selection based on the *rms* of a set of receiver functions from neighboring stations. Using these criteria, about 10,000 highest-quality receiver functions were deemed acceptable for the final migration.

**Receiver function calculation and migration.** The receiver functions were computed using the time-domain iterative deconvolution method (*S1*) with 100 iterations. The receiver functions were migrated using the common conversion point method (*S2*) using a 2D velocity model binned and averaged in 20° back-azimuth sectors (in order minimize the effects of 3D structure and uneven azimuthal distribution of the earthquakes used for receiver functions), and projected onto a linear profile along 85°E. The migration grid size was 1×1 km. The 2D velocity model was constructed taking into account station elevation, rough crustal thickness and velocities (*S3*, *S4*),  $V_p/V_s$  ratio and the Ganges Basin (*S3*). A horizontal smoothing filter of 3 and 5 km for the PS and multiple phases, respectively, was applied to the migrated images (Fig. S2).

Initial receiver function migration was performed using 1D velocity models for Nepal and Tibet (S3, S4). The migration of the PS phase and one of the multiple phases (here the PpS) yields two images of the crust-mantle boundary but not necessarily at the same depth. The difference in apparent depth of the Moho on the two images can be used to estimate the value of the average  $V_p/V_s$  of the crust along the profile (Fig. S3). This curve and the initial estimate of Moho geometry allow us to construct a 2D velocity model used for the final migrations (Fig. S2).

Fluids (aqueous or melt) modify the compressional ( $V_p$ ) and shear wave ( $V_s$ ) velocities, and increase the  $V_p/V_s$  velocity-ratio of a rock from its average 1.73 value (S5). Our results show (Fig. S3) that deviations in  $V_p/V_s$  from this value occur only in the Ganges Basin and in the Himalaya, which we explain by the presence of a thick sedimentary cover (S3) and felsic rocks, respectively. In Tibet, the  $V_p/V_s$  values stay in the regular range, and do not support the presence of widespread partial melt of the crust.

Using the 2D velocity model, the receiver functions are migrated three times, first assuming that the conversions are PS phases from the discontinuities and then assuming that they are PpS and PsS multiples (Fig. S2 (A) and (B), respectively). The PS migrated image shows the Moho (red) clearly, except in Nepal and in the BNS zone. Clearly visible are also local low-velocity zones (blue) in the Tibetan upper crust. The MU image (summing PpS and PsS migrations) clears up the Moho signal in Nepal, and reveals the interface duplex beneath the Lhasa Block. However, the upper crustal part of MU (about 10 km in Nepal and 15 km in Tibet) image cannot be interpreted due to the presence of PS phases migrated to shallower

depths. Finally, we combined the obtained PS and PpS and PsS images using a procedure of Wilson and Aster (S6, S7), which enhances features coherent in all three images.

### References and notes

- S1. J. Ligorria, C. J. Ammon, *Bull. Seismol. Soc. Am.* **89**, 1395-1400 (1999).
- S2. e.g., L. P. Zhu, *Earth Planet. Sci. Lett.* **179**, 183-190 (2000).
- S3. G. Hetenyi, R. Cattin, J. Vergne, J. L. Nábělek, *Geophys. J. Int.* **167**, 1106-1118 (2006).
- S4. S. S. Haines *et al.*, *Tectonics* **22**, 1001 (2003).
- S5. T. Watanabe, *Geophys. Res. Lett.* **20**, 2933-2936 (1993).
- S6. E. Kanasewich, *Time sequence analysis in geophysics* (The Univ. of Alberta Press, 364 pp., 1973).
- S7. D. Wilson, R. Aster, *J. Geophys. Res.* **110**, B05306 (2005).

### Figure legends

**Figure S1. (Top)** Theoretical receiver function showing the direct P wave and the converted waves (PS, and multiples PpS and PsS) for the case of a positive (increasing) impedance (velocity×density) contrast with depth at an interface below the station. **(Bottom)** Travel paths of the direct and converted waves from a P wave incident at the base of the interface. Capital and lower case letters denote upward and downward propagating legs, respectively. Thicker lines indicate propagation as P waves and thinner lines propagation as S waves. The amplitude of the conversion depends on the wave incidence angle at the interface and the impedance contrast across it.

**Figure S2. (A)** Image of interfaces along an 85°E line from receiver functions migrated assuming they are PS conversions. Red and blue colors correspond to the positive and

negative impedance contrasts, respectively. **(B)** Migrated image derived assuming the receiver functions represent the multiple phases, summing the PpS and PsS migrations. This image amounts to a vertical “shrinking” of the previous image, putting the PpS and PsS phases to the correct depth. See text for interpretation.

**Figure S3.** Average  $V_p/V_s$  values of the crust along  $85^\circ\text{E}$ . The curve is derived from 1D migration of the PS and PpS phases from Moho, and is represented only in those regions where both phases could be picked accurately. The regular value of  $V_p/V_s$  does not support the hypothesis on the presence of widespread partial melt in the Tibetan crust.

**Figure S4. (Top)** In search for uppermost mantle structure, PpS–PsS migrations along the main array plotting only negative conversions, since these seem to show most coherent signal. We see no strong conversions but there is clear change in the mantle fabric from predominantly north-dipping (presumably Indian mantle) to predominantly south-dipping (presumably Eurasian mantle) lineaments at about  $31^\circ\text{N}$ . **(Bottom)** Line drawing of the most prominent lineaments.

